Water and Gas Flooding Oil Monitored by a Realtime Unet-Neural-Network-Based Method

Jie Zhang , Maolei Cui * , Rui Wang

Posted Date: 25 March 2026

doi: 10.20944/preprints202603.1920.v1

Keywords: deep learning; flooding; dielectric constant; conductivity; real-time imaging; ground penetrating radar

 doi:10.20944/preprints202603.1920.v1

Article

Water and Gas Flooding Oil Monitored by a Realtime Unet-Neural-Network-Based Method

Jie Zhang [1,2], Maolei Cui [1,2,*] and Rui Wang [1,2]

[1] State Key Laboratory of Shale Oil and Gas Enrichment Mechanisms and Effective Development, Beijing 102206, China

[2] SINOPEC Petroleum Exploration and Production Research Institute, Beijing 102206, China

* Correspondence: cuiml.syky@sinopec.com

Abstract

To achieve real-time and accurate detections of residual oil distribution during water or CO_2 flooding, this study utilizes the high-frequency Ground Penetrating Radar (GPR) for monitoring of the flooding process in real time. The U-Net neural networks are trained to invert for the subsurface dielectric constants and conductivity distributions. The study first utilizes the gprMax forward tool to simulate the dynamic response changes of rock electrical parameters during flooding and constructs a high-resolution training dataset of 100,000 samples. Each sample contains the relationships between a subsurface electrical parameter model and its corresponding multi-transmitter, multi-receiver GPR responses. A deep learning inversion network based on the U-Net architecture is trained to extract multi-scale features through an encoder-decoder structure, achieving an end-to-end mapping from GPR echo signals to subsurface electrical parameters. Numerical and physical core experimental results show that the method accurately inverts the electrical parameter distributions of the oil, water, and gas in the sandstone model, successfully capturing the position and morphology changes of the displacement front. The average relative error of dielectric constant inversion is controlled within 5%, with the error mainly concentrated in high-conductivity water regions for conductivity inversion results. Compared to traditional full waveform inversion methods, the proposed approach offers a fast inversion solution and is less affected by the initial model and noise. The results reveal the feasibility and superiority of the neural network based deep learning method in GPR electromagnetic inversion, providing a new method for real-time flooding monitoring and intelligent reservoir development during oil and gas flooding.

Keywords: deep learning; flooding; dielectric constant; conductivity; real-time imaging; ground penetrating radar

1. Introduction

In the field of unconventional oil and gas development, improving oil recovery has always been a crucial issue (Gao et al., 2024). Water or CO_2 injection to displace residual oil is a common enhanced oil-recovery method, and its efficiency is closely related to the distribution of multiphase fluids in the reservoir (Song et al., 2025). There are several methods usually utilized to monitor the distribution of the multiphase fluids in the flooding process. Traditional multiphase-fluid-detection methods, such as electric well logging, nuclear magnetic resonance, and CT imaging, although able to detect fluid distribution and pore structure to some extent, are generally limited by their resolutions, experimental complexities, or low sensitivity to water, gas, or oil, and make real-time precise fluid migration investigation difficult (Kleinberg, 2001; Wildenschild, 2013). However, the electrical parameters of water, gas, and oil, such as their conductivity and dielectric constant, are different, and they are useful to determine the distributions of oil, water, and gas during the flooding process, thereby laying the foundation for understanding the migration phases in the rock. Further, these

 doi:10.20944/preprints202603.1920.v1

parameters provide insights into the dynamic changes of fluid saturations in the flooding process, which are critical for optimizing recovery strategies (Archie, 1942).

The Ground Penetrating Radar (GPR) is a non-contact, non-destructive detection technique based on the propagation principles of high-frequency electromagnetic waves. It is highly sensitive to electrical parameters such as conductivity and dielectric constant and is characterized by high resolution, moderate penetration depth, and fast response time. During CO_2 or water flooding oil in reservoirs, the saturation of oil, water, and gas in the pore structure changes, leading to variations in the dielectric constant and conductivity parameters. These changes also lead to changes in the acquired GPR response data. Thus, it is an effective approach for studying water- or gas-flooding oil processes in rock samples (Bradford, 2008; Cassidy, 2009). It has been increasingly used in the monitoring of rock electrical properties during oil reservoir displacement processes.

Inversion results of the distributions of conductivity and dielectric constant from the acquired GPR response data are usually utilized to reveal the changes of electrical parameters in the flooding process. However, the inversion problem of conductivity and dielectric constant from the acquired GPR response data is a typical nonlinear and ill-posed problem. There are several different inversion methods. Traditional inversion methods, such as finite-difference backpropagation (FD-BP), Newton's method, and full waveform inversion (FWI) (Zhen et al., 2025), typically rely on forward modeling and gradient optimization frameworks, iterating to minimize the difference between observed and simulated data to obtain the optimal model. Although these methods can theoretically achieve detailed electrical parameter distribution images, they have evident limitations: first, high computational cost and low inversion efficiency, as each iteration of inversion requires a high-precision forward simulation, which increases time consumption, makes it difficult to meet real-time processing demands in field applications; secondly, these methods are highly sensitive to the initial model and prior information, which may lead to local optima and unstable inversion results (Zhang et al., 2023); thirdly, when facing complex media, multiphase systems, or noisy observational data, traditional methods show poor robustness and difficulty ensuring inversion accuracy and repeatability.

However, deep learning-based inversion methods can solve the above issues and have gained much attention in recent years. Unlike traditional physics-driven methods, the deep learning method is driven by a large amount of data, capable of automatically learning complex nonlinear relationships between input (GPR responses) and output (electrical parameters) from a large number of samples. Deep learning method has several advantages in electromagnetic parameter inversions: first, fast inference speed, as only one forward propagation is required for inversion prediction, meeting real-time requirements; secondly, strong nonlinear fitting ability, capable of approximating complex electromagnetic propagation and reflection mechanisms; thirdly, robustness to noise and ease of integrating multi-source information; fourthly, support for end-to-end training, eliminating the need for cumbersome forward calls and gradient calculations. The U-Net neural network is a typical fully convolutional deep-learning architecture, which is widely used for imaging semantic segmentation tasks. Its encoder-decoder structure has excellent feature-extraction capabilities and spatial restoration capabilities, making it particularly suitable for mapping GPR signals into high-resolution parameter distribution images (Chen et al., 2024). Therefore, this study develops a deep-learning-based inversion method based on the U-Net neural network to discover the electrical parameters.

In this study, we develop the U-Net-based inversion method by utilizing numerical GPR responses. An open-source three-dimensional (3D) GPR forward simulation tool, gprMax, based on the Finite-Difference Time-Domain (FDTD) method, supports high-precision modeling and simulation of complex geometries and multi-physical parameter settings, and makes it suitable for simulating the GPR signal propagation and reflection process in rock media (Warren et al., 2016). This study uses gprMax to model the electrical parameter changes in rocks under different flooding conditions (water and CO_2 injection) and generate a large amount of GPR responses as a training dataset for the inversion model. First, construct rock media models with water and CO_2 injections.

 doi:10.20944/preprints202603.1920.v1

Then, we simulate GPR responses at different stages and generate a large number of labeled sample datasets. Finally, we design and train a deep neural network model based on the U-Net architecture to achieve an end-to-end imaging method from GPR responses to 2D conductivity and dielectric constant distribution images. Moreover, the neural network is also tested in the physical core experiments.

In the following part of this study, we introduce the method to prepare the datasets for training the network in the section 2. Section 3 introduces how to train the U-net based neural network, and Section 4 shows the performance of the network on monitoring different flooding processes, and the physical core experiments.

2. Methodology and Datasets for Network Training

Deep learning (DL) methods can directly learn the relationship between observed GPR responses and subsurface electrical parameter distributions in a data-driven training framework, and enables to reach fast and stable inversion results (Zhang et al., 2023; Meng et al., 2025). In the deep learning inversion framework of this study, we first use electromagnetic forward simulation tools (e.g., gprMax) to generate a large-scale training dataset. Each data set consists of input and output parts: the input part is typically time-domain electric field responses from multiple transmitter-receiver pairs, and the output part corresponds to 2D subsurface medium parameter distributions, such as conductivity and dielectric constant.

The forward modeling of GPR datasets can be described by Maxwell's equations. Assuming electromagnetic waves propagating through an isotropic, non-source medium, the propagation law can be expressed as follows (Liu et al., 2025)

$$\nabla \times E = -\mu \frac{\partial H}{\partial t}, \nabla \times H = \sigma E + \epsilon \frac{\partial E}{\partial t}\ , \tag{1}$$

where E and H are the electric and magnetic field vectors, ϵ is the dielectric constant, μ is the permeability, and σ is the conductivity. The spatial variations in the medium parameters directly affect wave propagation speed, attenuation, and reflection intensity of electromagnetic fields.

In this study, gprMax is used to do the forward modeling and to generate the training data required for deep learning inversion. By changing the distributions of oil, gas, and water in the core, and producing a variety of electrical parameter sets, a large amount of corresponding radar response data can be simulated by the gprMax software. Each data set includes the excitation signal from the transmitter, time-domain electric field responses from the receiver, and the corresponding two-dimensional (2D) electrical parameters.

As an example of the GPR measurement scheme shown in Figure 1, the transmitter is located at the upper boundary of the 2D model, with a spacing of 0.05m, and 5-transmitter is distributed along the x-direction. The transmitter is oriented along the z-axis. The receivers are located at the opposite interface of the model, with 5 receivers of 0.05 m intervals along the x-direction. The transmitters and receivers are vertical electric dipoles. The waveform emitted from the transmitter is a Ricker wavelet with a center frequency of 1.5 GHz, the observation is set as follows, and 5 receivers simultaneously capture the transmitting signals from one transmitter. Moreover, one synthetic model consists of two horizontal media layers, with a horizontal interface at 0.15m. The upper layer is water, with the relative dielectric constant of 78.5 and the conductivity of 1 S/m. The lower layer is oil, with a relative dielectric constant of 2.2 and conductivity of $1 \times 10^{-10} S/m$. The simulated GPR responses by the gprMax are shown in Figure 2. It shows the simulated GPR responses are affected by the model medium, transmitter and receiver positions.

 doi:10.20944/preprints202603.1920.v1

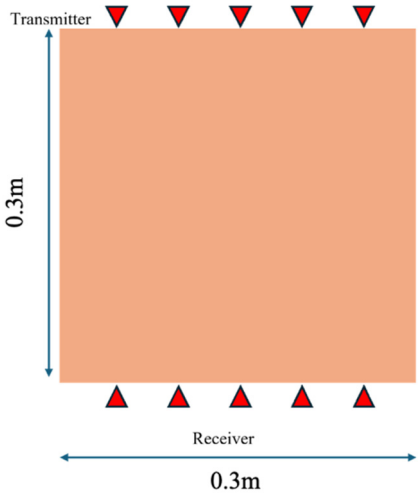

Figure 1. Measurement Setup. The orange region represents sandstone indicated. The red triangles denote the receiver and transmitter antennas.

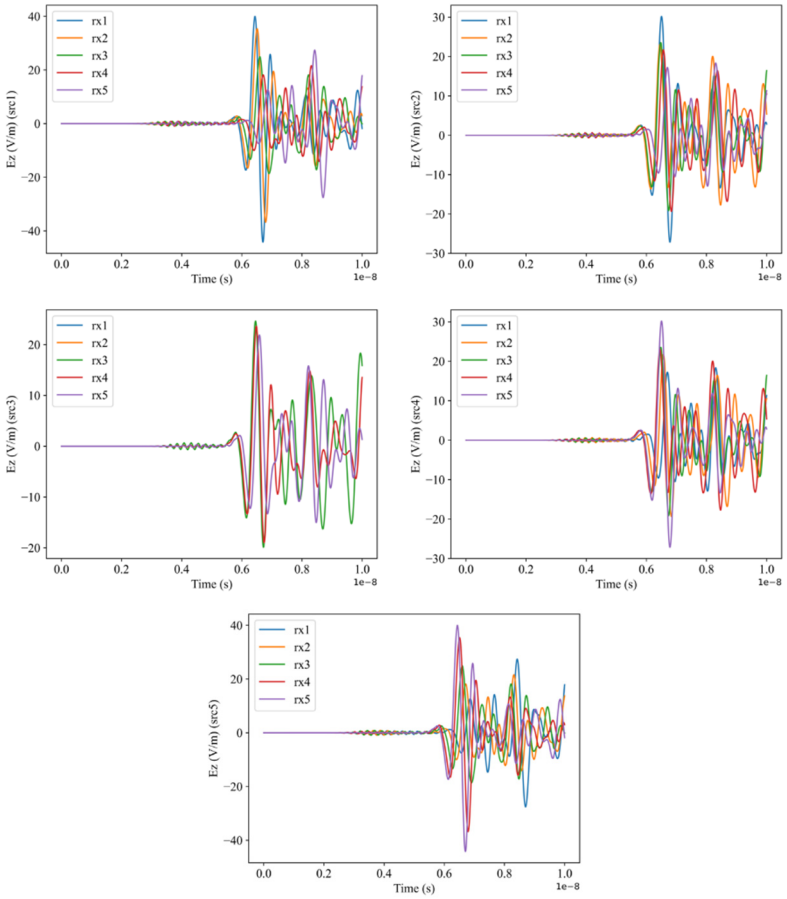

Figure 2. Forward simulation results from the gprMax software, where src1, src2, src3, src4, and src5 represent the first to the fifth transmitter antennas, and rx1, rx2, rx3, rx4, and rx5 represent the first to the fifth receiver antennas.

2.1. Vertical Flooding Datasets

For oil-bearing sandstone, the oil content is unsaturated. By injecting water from one end, the water-injected region can be estimated. The water flooding causes oil to accumulate ahead of the water front, where it is regarded as oil-saturated regions, and the foremost region is unsaturated oil regions. In this case, the water-saturated layer, oil-enriched layer, and unsaturated oil layer can be

 doi:10.20944/preprints202603.1920.v1

simulated as horizontal layers of different media. Figure 3 shows the distribution of different states of saturation during the waterflooding process.

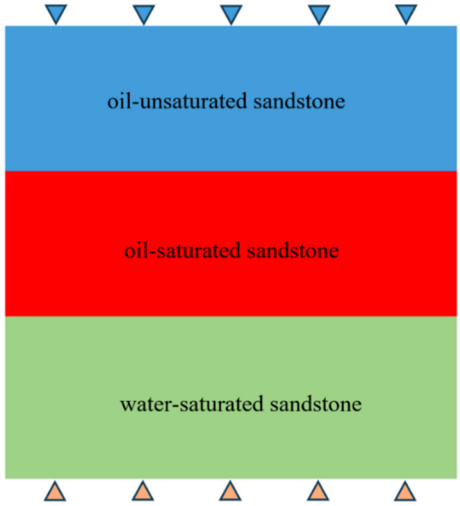

Figure 3. Distribution of different media states at different stages of flooding.

When creating different model sets, we use a random technique to set the depth of layer interfaces and electrical parameters such as conductivity and dielectric constant. A total of 100,000 models were created, and the variation range of different parameters is shown in Table 1. Data were collected using the device shown in Figure 1 to obtain the vertical electric field response data as input. When constructing the labeled data, we discretize the model into 900 (30×30) small blocks, each with corresponding dielectric constants and conductivity values. The label data includes relative dielectric constants and conductivity, both with the same dimensions. The responses from each model have 25 electric curves from different transmitter-receiver pairs, with a time sampling number of 1756. As a result, the input dimension of each model is $5 \times 1765 \times 5$.

Table 1. Value ranges and step sizes of different parameters.

Water		**Oil**		**Sandstone**		**Water-Oil Interface**	**Oil-Sandstone Interface**
Dielectric Constant	Conductivity	Dielectric Constant	Conductivity	Dielectric Constant	Conductivity	cm	cm
10～30	-2～0	2～6	-5～-3	6-10	-2～-1	10～40	10～40
1	0.1	1	0.1	1	0.1	1	1

2.2. Diagonal Flooding Datasets

By injecting water from one corner of the model and outputting oil or water in the diagonal corner, the water-injected region can also be estimated. The water flooding causes oil to accumulate ahead of the water front, and there are also water-saturated regions, water-oil mixed regions, and oil-saturated regions. In simulations, the study area is divided into 100 small blocks, each with a side length of 3 cm, and each block is assigned different conductivity and dielectric constant values to simulate different substances (water-saturated, oil-saturated, and unsaturated oil-water) at different flooding stages. The meshing of the synthetic model in the study is shown in Figure 4. Each block is randomly assigned dielectric constants and conductivity. A random method is used to determine the model parameters, with the value ranges and step sizes shown in Table 2. We created a total of 100,000 datasets. A randomly selected synthetic model as an example is shown in Figure 5. Figure 5 shows that it has a high conductivity and a high dielectric constant due to the water injection. Due to water

 doi:10.20944/preprints202603.1920.v1

flooding, oil accumulates in the center of the model, and it shows low conductivity and low dielectric constant properties. The responses from each model have 25 electric curves from different transmitter-receiver pairs, with a time sampling number of 1756. As a result, the input dimension of each model is $5 \times 1765 \times 5$.

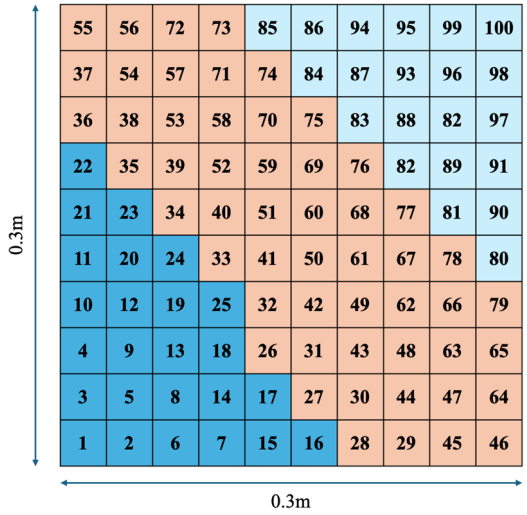

Figure 4. Simulation of different stages of oil-water flooding.

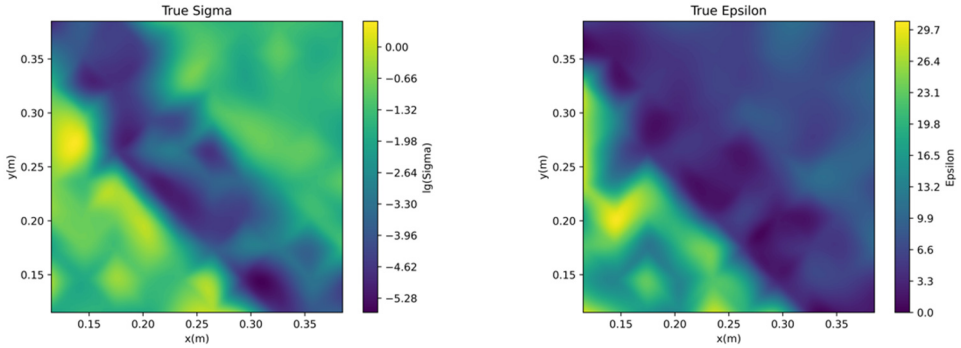

Figure 5. The conductivity and dielectric constant distribution map, where the left panel is about the logarithmic conductivity distribution and the right panel shows the dielectric constant distribution.

Table 2. Range of dielectric constants and conductivities for different substances (conductivity in logarithmic values).

Water		**Oil**		**Sandstone**	
Dielectric Constant	Conductivity	Dielectric Constant	Conductivity	Dielectric Constant	Conductivity
10～30	-2～0	2～6	-5～-3	6-10	-2～-1
1	0.1	1	0.1	1	0.1

To ensure the neural network performs well, we normalized the input and output data to the [0, 1] range using min-max normalization. The normalization formula is as follows:

$$x_{norm}^{i}=\frac{x^{i}-x_{min}^{i}}{x_{max}^{i}-x_{min}^{i}}. \quad (2)$$

where i indicates the position of an element within the array, and norm represents the normalized data, x refers to the input or output. The conductivity of water and oil requires a logarithmic transformation.

 doi:10.20944/preprints202603.1920.v1

To effectively prevent overfitting and ensure that the neural network performs well, the dataset is divided into three subsets: training, validation, and testing. The training set is used for training the neural network, the validation set is used to prevent overfitting during the training process, and the testing set is used to evaluate the generalization ability. The ratio of the number of samples in the three subsets is 81% for training, 9% for validation, and 10% for testing.

For conductivity and dielectric constant inversion, we created two datasets. The input data for each dataset are the same, but the output data differ. For dielectric constant inversions, the output data consist of the dielectric constant values for 100 blocks, while for conductivity inversions, the output data consist of the logarithmic conductivity values for the 100 blocks.

3. Neural Network Training

The training process of the network can be regarded as minimizing the loss function between the predicted model parameters and the true label parameters, commonly using metrics such as Mean Squared Error (MSE), Structural Similarity Index (SSIM), or multi-task weighted loss functions. Specifically, the deep neural network is controlled by trainable parameters, and its goal is to approximate the implicit relationship between the observed data and the electrical parameters. Through training on a large number of datasets, the neural network learns the high-dimensional nonlinear relationships from electromagnetic responses to subsurface electrical parameters, enabling direct prediction of 2D parameter distributions from real measurements. After sufficient training, the model is capable of rapidly performing inversion on measurement data.

In terms of network structure, this study adopts a 2D U-Net neural network to perform electrical parameter inversion of the flooding process based on GPR data. The U-Net neural network, with its typical encoder-decoder architecture, extracts spatial features from the subsurface medium through multi-scale convolutions and uses skip connections to preserve both shallow details and deep semantic features during the inversion process. This neural network is particularly suitable for detecting the spatial electrical contrasts of oil and water and the subtle changes in the interfaces during waterflooding. As flooding progresses, the conductivity of the water-saturated zone changes, and the dielectric constant changes with saturation.

The U-Net neural network inversion method requires only a single forward modeling, significantly improving computational efficiency. Moreover, the multi-scale characteristics enable it to recognize spatial variations in the flooding front, allowing for fine characterization of the oil-water or gas-oil interface migration process. Therefore, its characteristics, such as spatial feature extraction and information fusion capabilities, are well-suited to discover the physical features of the waterflooding dynamics observed by GPR, making the neural network highly efficient in inversion and real-time monitoring of reservoir evolution while maintaining low computational complexity.

3.1. Neural Network Structure

This study constructs a deep neural network based on the U-Net architecture, as shown in Figure 6, to perform 2D inversion and then to reconstruct subsurface electrical parameters from GPR data. The network is trained using supervised learning, with a large amount of GPR data and corresponding geological models. The encoder part gradually extracts high-level features through multiple convolution and pooling operations, capturing spatial variation patterns at different scales. The decoder part uses deconvolution and skips connections to progressively restore spatial resolution, effectively reconstructing detailed information. The skip connection mechanism ensures that low-level features, such as interface morphology and local reflection intensity, which are preserved during the decoding stage, and improves the accuracy of layer boundary recognition. It outputs the corresponding 2D conductivity or dielectric constant distributions. During neural network training, the batch size is set to 128, and the number of training epochs is 200. The U-Net uses the hyperbolic tangent function (Tanh) as the activation function, as shown in Table 3. To prevent overfitting and improve its generalization ability, a regularization term is introduced into the L2 loss function. The Adam optimization algorithm is employed to enhance the training efficiency of

 doi:10.20944/preprints202603.1920.v1

the neural network (Kingma, 2014). The neural network architecture is built using the PyTorch-GPU framework (Paszke et al., 2019), and training and testing are performed using an Nvidia GeForce RTX 3060 GPU.

After the training is finished, we could utilize the U-Net network structure to automatically extract spatial features from the GPR data, and achieve an end-to-end output from GPR response data to subsurface electrical parameter distributions.

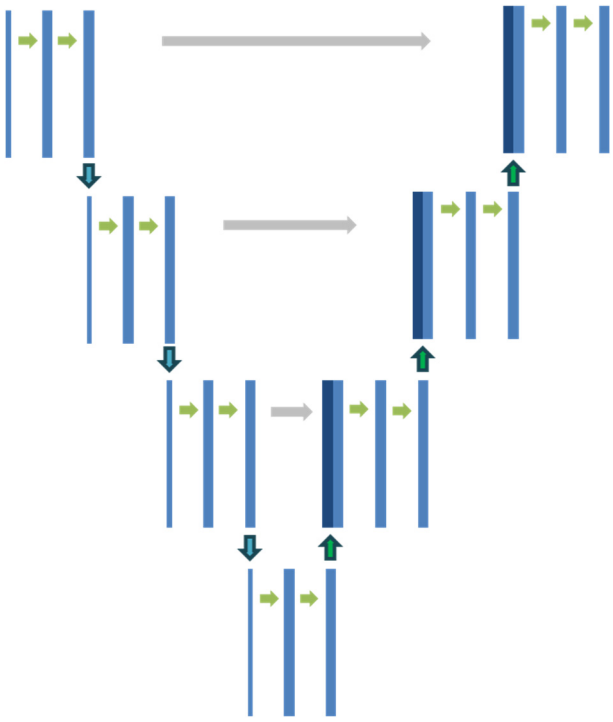

Figure 6. Schematic diagram of the U-Net neural network structure.

Table 3. Neural Network Hyperparameters.

Learning Rate	Batch Size	Epochs	Activation Function	Optimization Algorithm	Regularization
1E-4	128	200	Tanh	Adam	L2

3.2. Training Process

For each dataset, we trained two identical neural networks, one for the inversion of the relative dielectric constant and another for the conductivity. The training process is illustrated in Figure 7. Since we have two types of output datasets, we trained two sets of neural networks, corresponding to the inversion of dielectric constant and conductivity.

The neural networks for resistivity and dielectric constant inversion were trained. The loss function decay curves in the training process for dataset 1 are shown in Figure 8, and those for dataset 2 are shown in Figure 9. As the number of training epochs increases, both the training and testing loss functions quickly decrease and converge to a minimum value. After 100 epochs, although the training set loss continues to decrease, the validation loss has already converged. To prevent overfitting and ensure the network's generalization ability, we stopped the training at 200 epochs and used the neural network trained at this point as the final inversion model. Under a GPU-based architecture, the training time of all neural networks is approximately 2800 seconds.

 doi:10.20944/preprints202603.1920.v1

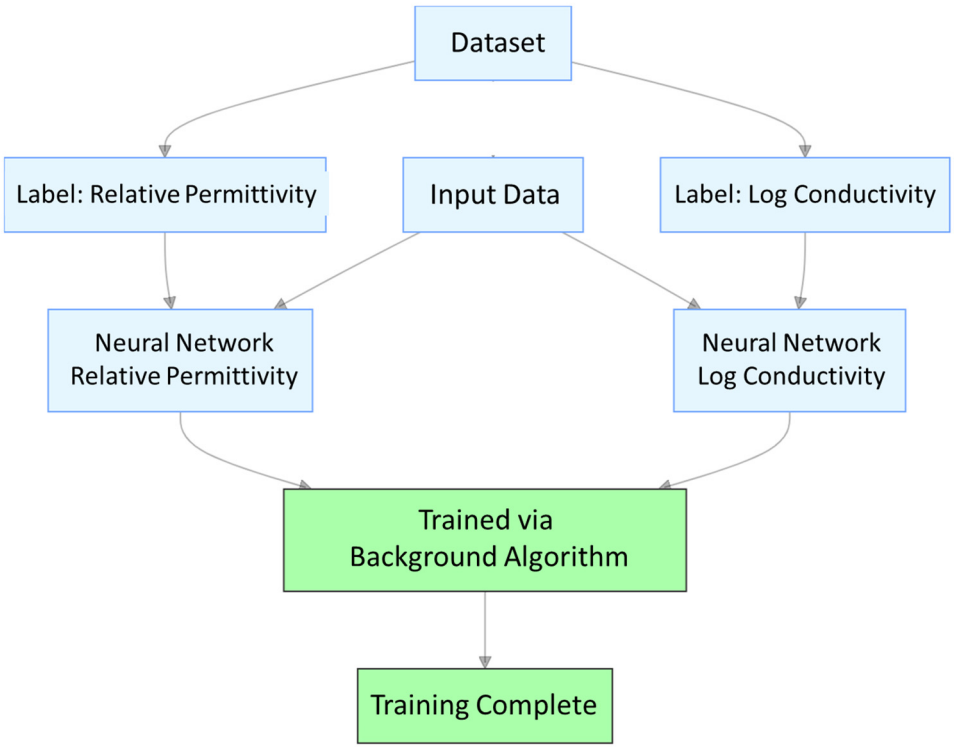

Figure 7. Inversion neural network training flowchart.

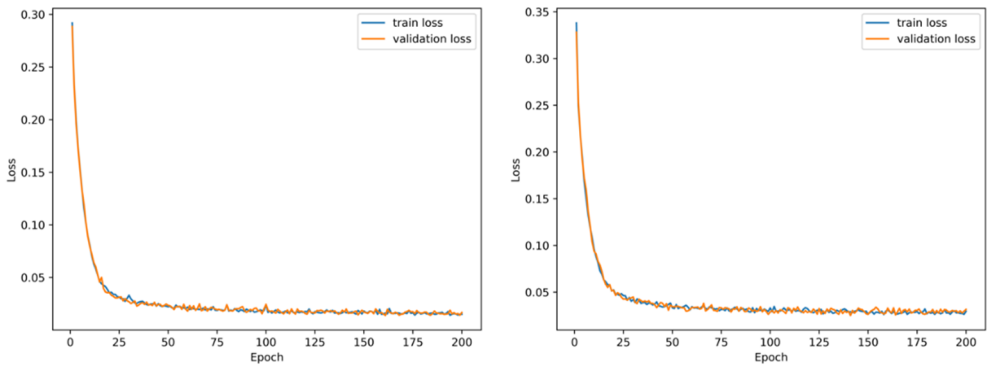

Figure 8. Loss function decay curves for Dataset 1. The left graph shows the decay curve for the dielectric constant inversion network, and the right graph shows the decay curve for the resistivity inversion network.

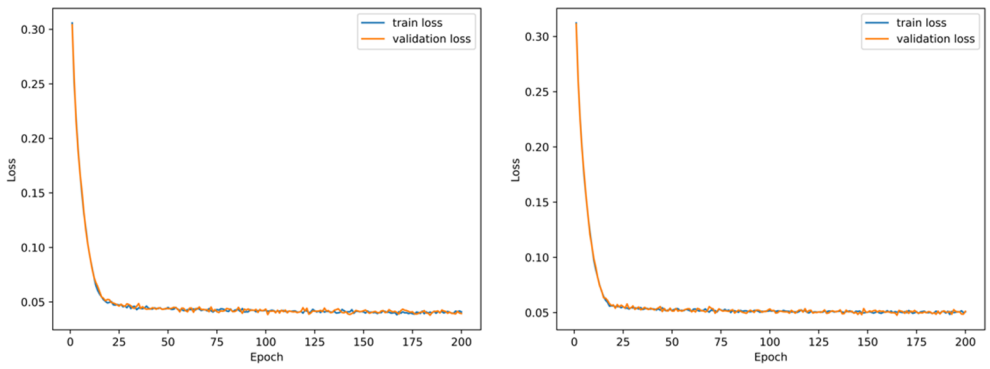

 doi:10.20944/preprints202603.1920.v1

Figure 9. Loss function decay curves for Dataset 2. The left graph shows the decay curve for the dielectric constant inversion network, and the right graph shows the decay curve for the resistivity inversion network.

4. Inversion Results from the U-Net Neural Network

4.1. Vertical Flooding Inversion

The trained inversion neural network was tested using the testing dataset from Dataset 1. We estimate the relative error as a quantitative indicator to evaluate the inversion performance. Figures 10 and 11 show the inversion results of several different models. The 2D inversion results for the dielectric constant are shown in Figure 10, and the inversion results for conductivity are shown in Figure 11. As can be seen, the neural network can accurately invert the dielectric constant and conductivity variations for different layers and can also precisely identify the interface positions. However, the relative error distribution shows that large errors occur at the interface boundaries. This may be related to the large sampling interval when discretizing the 2D medium.

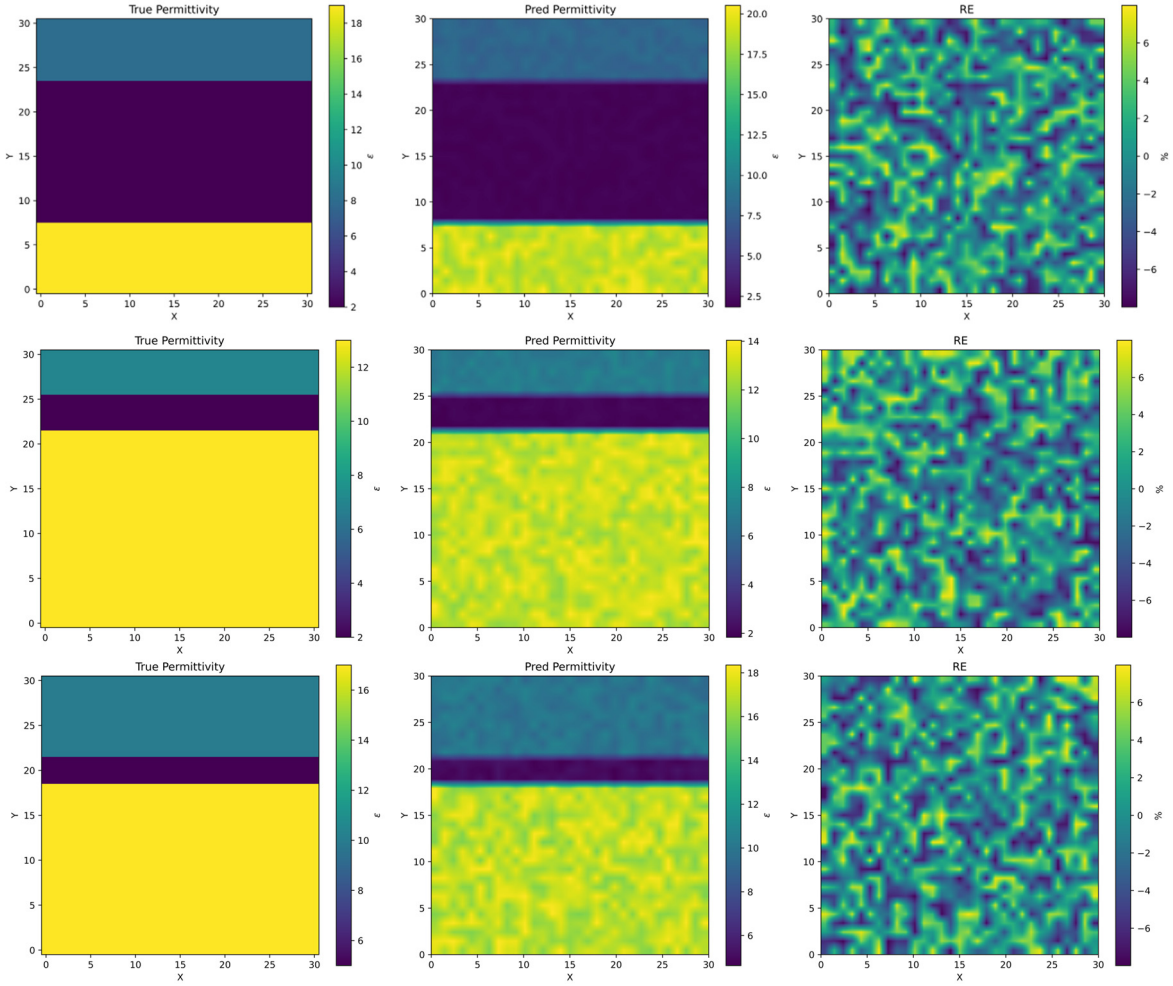

Figure 10. 2D dielectric constant inversion results of 3 randomly selected synthetic models, where the first, second, and third layer is from 3 models, and the first, second, and third column is the true dielectric constant, inversion results, and the relative errors, respectively.

 doi:10.20944/preprints202603.1920.v1

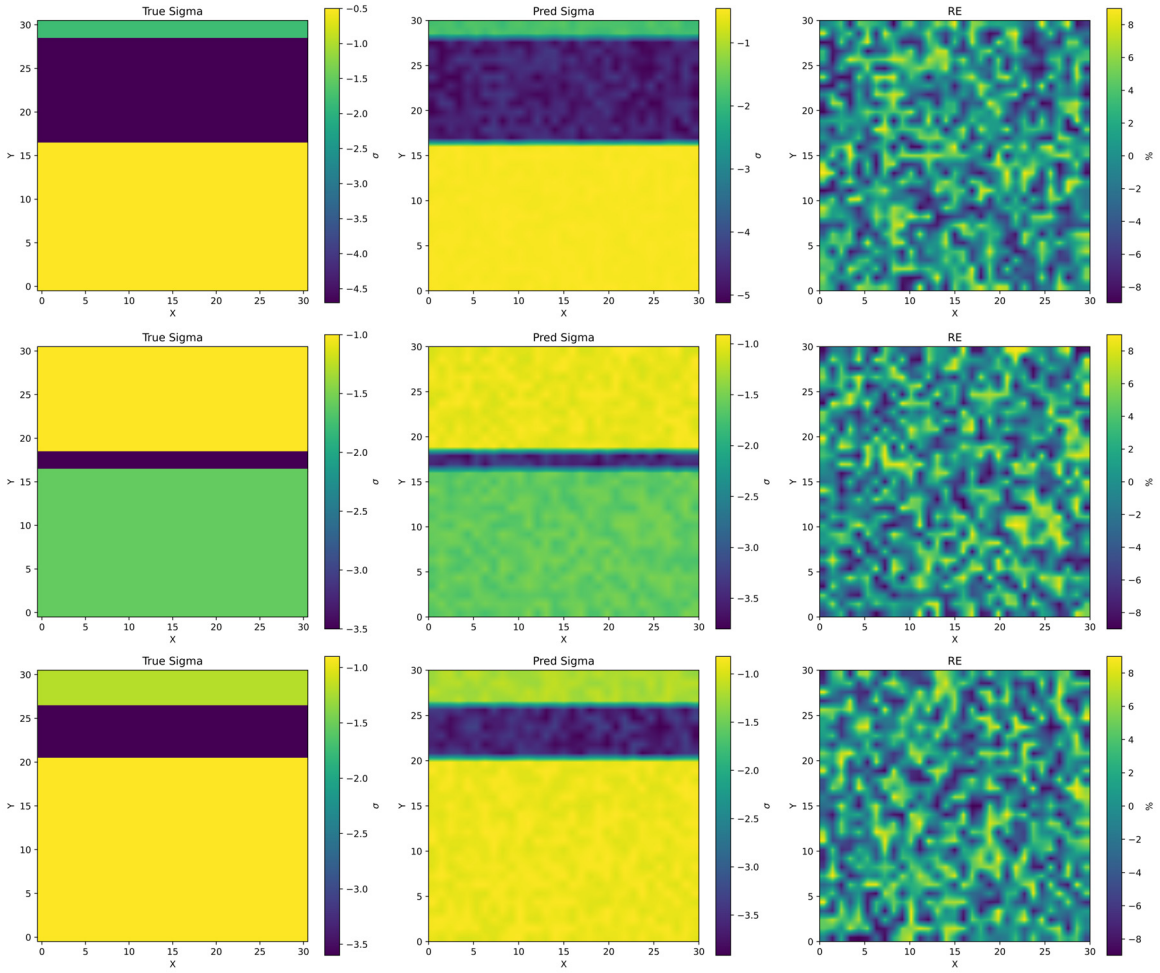

Figure 11. 2D conductivity inversion results for the model of 3 randomly selected synthetic models, where the first, second, and third layer are from 3 models, and the first, second, and third column is the true conductivity, inversion results, and the relative errors, respectively.

4.2. Diagonal Flooding Inversion (Oil-Water Flooding)

The trained inversion neural network was tested by using the testing dataset, and the relative error was calculated as a quantitative indicator for evaluating inversion performance. We randomly selected inversion results. The 2D inversion results for the dielectric constant are shown in Figure 12, and the inversion results for conductivity are shown in Figure 13.

As shown in Figure 12, the neural network can accurately invert the dielectric constant value variations and can precisely recognize the water-oil and oil-sandstone interfaces. The relative error distribution shows that only a few points exhibit larger relative inversion errors. Figure 13 indicates that the neural network also performs well in inverting conductivity, although the large errors are slightly larger compared to the dielectric constant.

 doi:10.20944/preprints202603.1920.v1

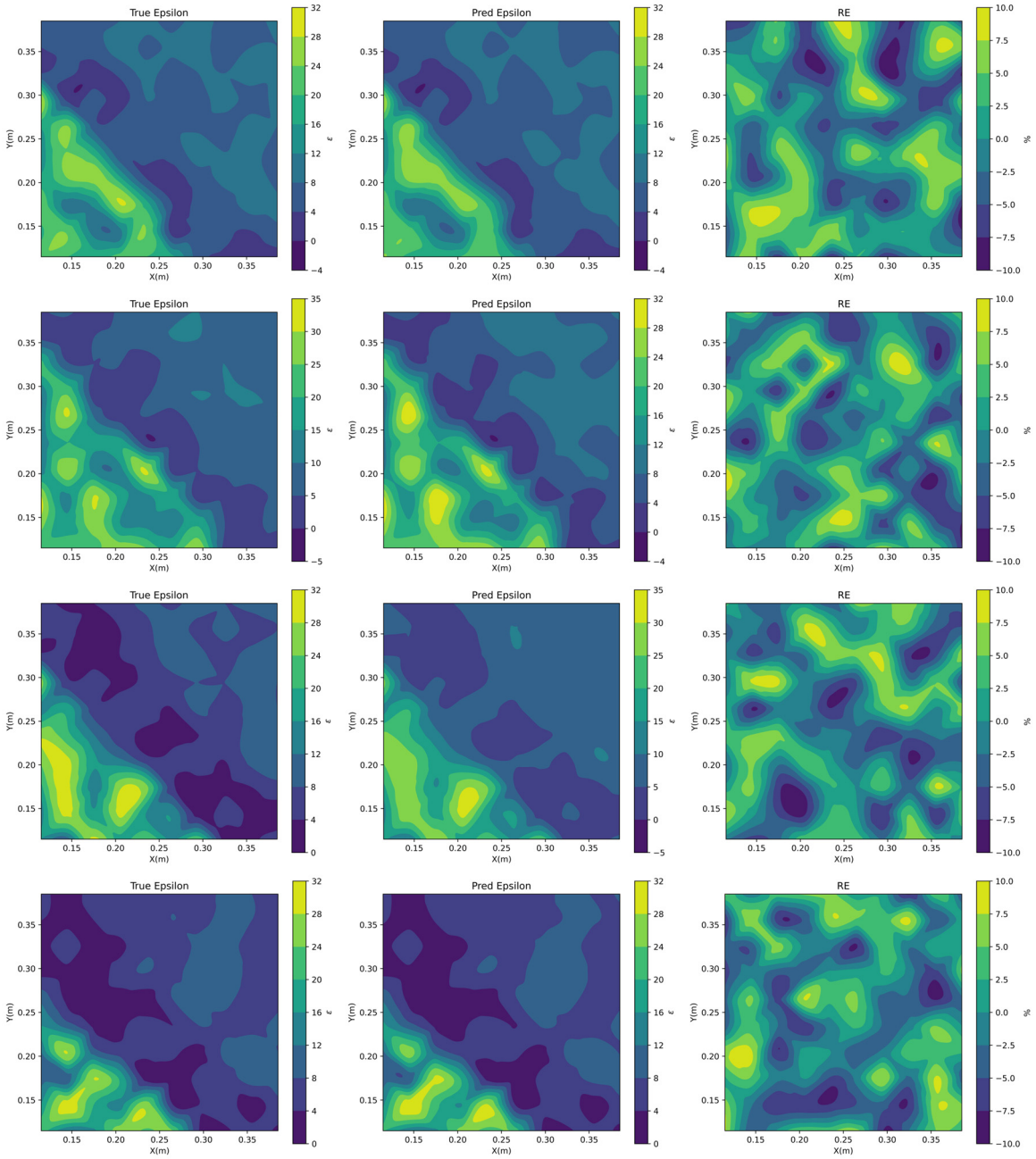

Figure 12. 2D dielectric constant inversion results for the model. Each row of three images represents the inversion results for different models. The left column image shows the true dielectric constant distribution, the middle column image shows the inverted dielectric constant distribution, and the right column image shows the relative error distribution of the inversion results.

 doi:10.20944/preprints202603.1920.v1

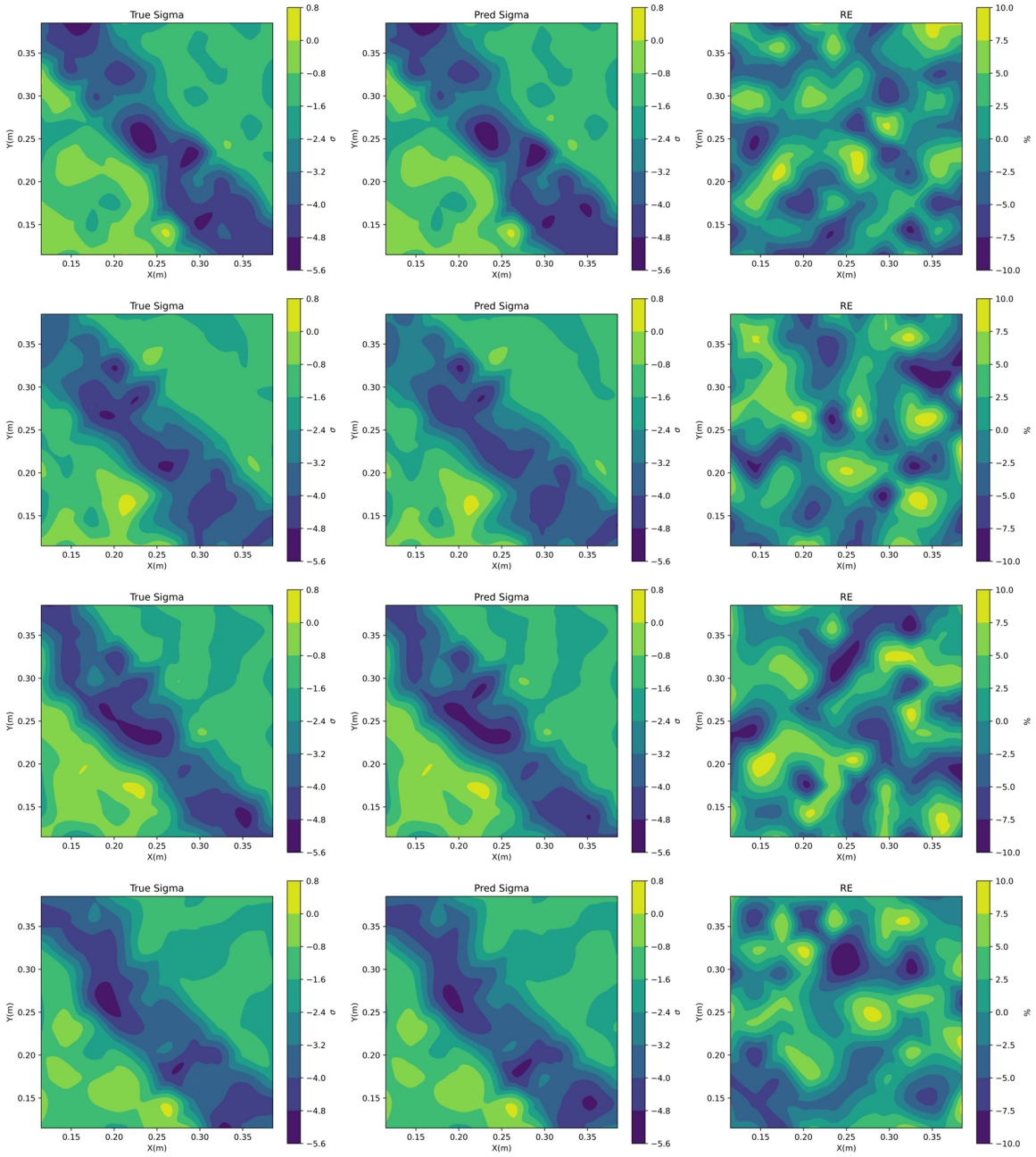

Figure 13. 2D conductivity inversion results for the model. Each row of three images represents the inversion results for different models. The left column image shows the true conductivity distribution, the middle column image shows the inverted conductivity distribution, and the right column image shows the relative error distribution of the inversion results.

To further evaluate the inversion accuracy, we statistically analyzed the average relative errors of the inversion results for 10,000 models as shown in Figure 14. The dielectric constant inversion errors are smaller than ±8%, but the error is slightly higher for low dielectric constant values in the oil region. For low conductivity regions (oil and sandstone), the inversion results are relatively accurate, with errors within 10%. For high conductivity regions (water), the inversion results have a little large errors.

 doi:10.20944/preprints202603.1920.v1

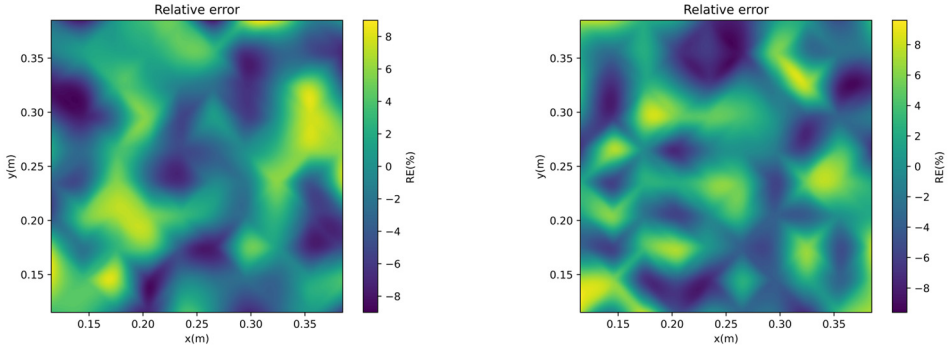

Figure 14. Average relative error distribution for the inversion results of the testing set. The left graph shows the relative dielectric constant, and the right graph shows the relative conductivity.

4.3. Diagonal Drive Simulation Inversion (Oil-Gas-Water Flooding)

The trained inversion network was evaluated using the simulated flooding model, and the spatial distributions of the relative error (RE) are shown in Figure 15. The color scale in both panels ranges approximately from −8% to 9%, indicating that the majority of inversion errors remain within a relatively narrow interval.

The left panel illustrates the spatial distribution of the relative error for the first inverted parameter. The error field exhibits a mixed pattern of purple and yellow regions, indicating the coexistence of slight underestimation and overestimation. Most areas are characterized by moderate colors, suggesting that the inversion error is generally small and spatially stable. Localized negative errors (purple tones) appear sporadically in several regions, particularly around the central part of the model (x ≈ 0.20–0.30 m, y ≈ 0.22–0.30 m), indicating slight underestimation in these heterogeneous zones. Positive errors (yellow tones) are distributed in scattered patches, reflecting limited local overestimation. Overall, the absence of large contiguous extreme-error regions demonstrates that the inversion network effectively captures the spatial variation of the physical parameter and maintains good reconstruction accuracy.

The right panel shows the relative error distribution for the second inverted parameter. Compared with the left panel, the spatial pattern appears slightly smoother but follows a similar error magnitude range. The map is dominated by orange and light-purple colors, suggesting that most inversion results deviate only slightly from the true values. Regions of positive error (yellow tones) are mainly distributed in the right half of the model (x ≈ 0.25–0.35 m), indicating mild overestimation, while negative errors (dark purple) occur intermittently near the upper-left region. Despite these localized deviations, the overall error amplitude remains small, and no significant systematic bias is observed.

In general, both error maps demonstrate that the trained neural network achieves stable inversion performance across the entire spatial domain. The relative errors are mostly confined within ±8%, and the spatial continuity of the reconstructed parameters is well preserved, indicating that the network effectively learns the mapping relationship between the electromagnetic responses and the subsurface physical parameters.

Moreover, we randomly present the inversion results of several models as shown in Figures 16 and 17. It reveals that the inversion of relative permittivity enables more accurate delineation of the interface between water and oil-gas, while the inversion of electrical conductivity can more precisely reveal the interface between oil and gas.

 doi:10.20944/preprints202603.1920.v1

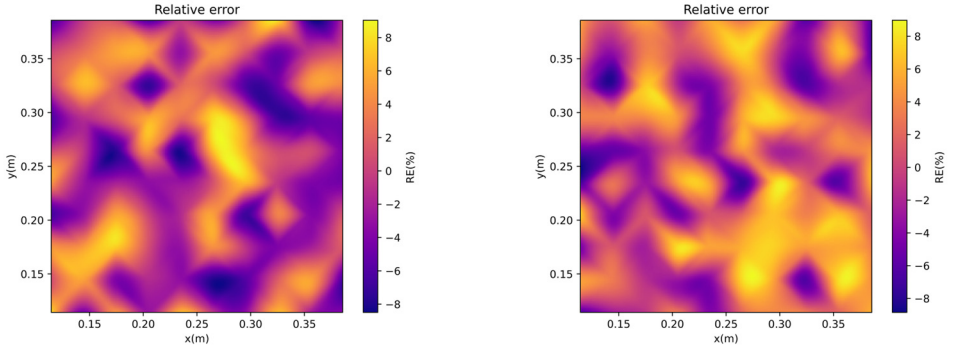

Figure 15. Spatial distribution maps of average relative error for the test set. The left panel corresponds to the relative errors of the permittivity, and the right panel is about that of the electrical conductivity in the logarithm scale.

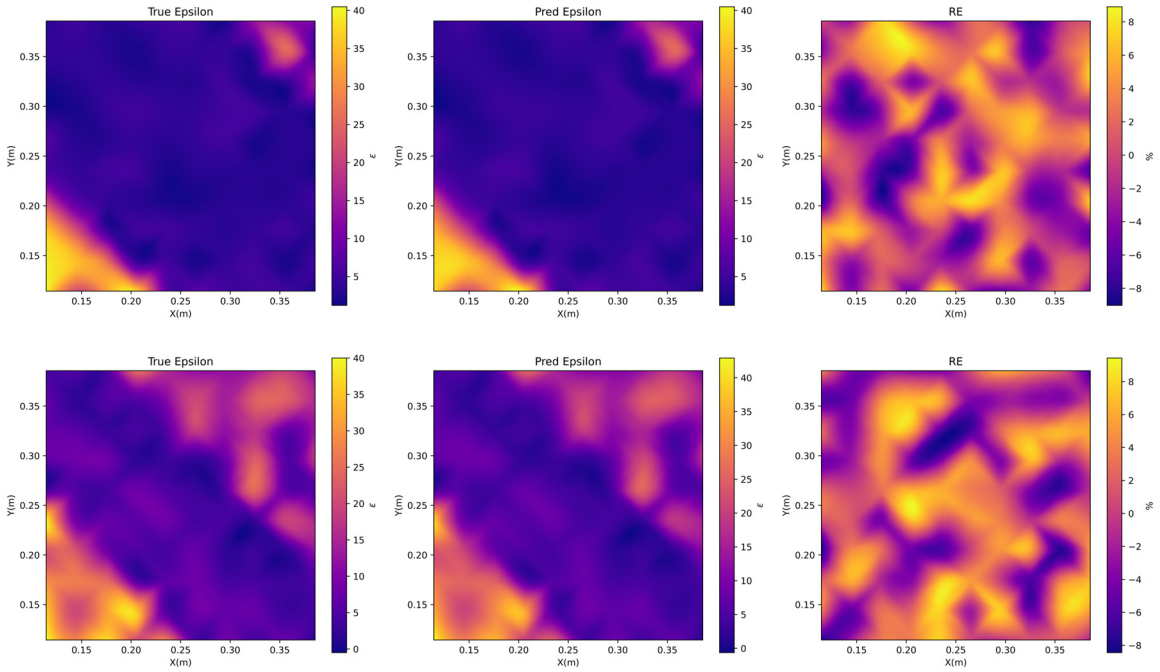

Figure 16. 2D inversion results for a random model. Each row of three images represents the inversion results for different models. The left image shows the true distribution, the middle image shows the inverted distribution, and the right image shows the relative error distribution of the inversion results. The first row is about the distributions of permittivity, and the second row is about the conductivity distributions.

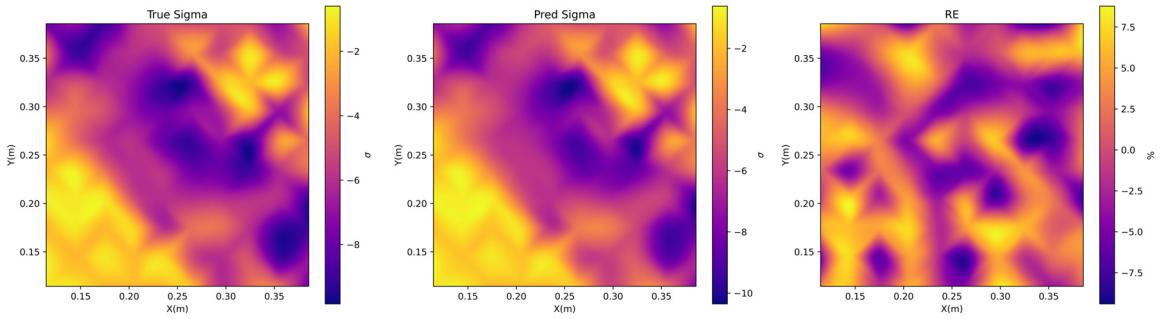

 doi:10.20944/preprints202603.1920.v1

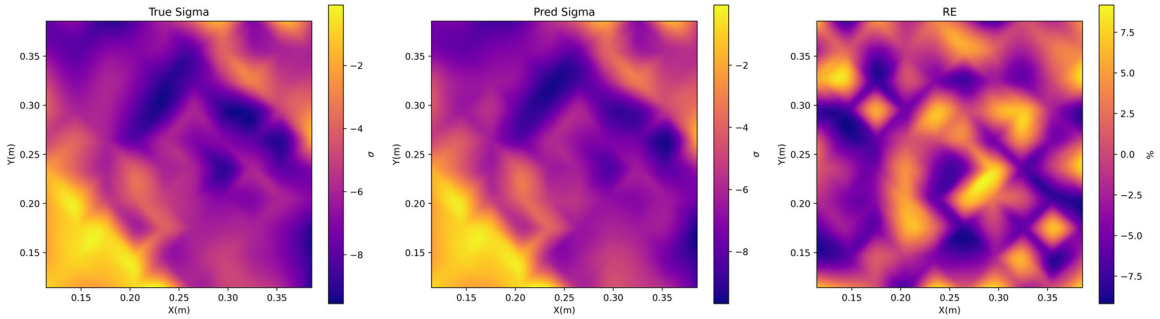

Figure 17. 2D inversion results for another random model. Each row of three images represents the inversion results for different models. The left image shows the true distribution, the middle image shows the inverted distribution, and the right image shows the relative error distribution of the inversion results. The first row is about the distributions of permittivity, and the second row is about the conductivity distributions.

4.4. Physical Core Flooding Experiments

To further test the performance of the proposed method in measuring the physical core flooding experiment, a flooding experiment was conducted. The experiment was done with 12 transmitters and 12 receivers as shown in Figure 18.

Figure 19 shows the starting stage of water flooding oil, and all the figures are characterized by a low conductivity value and a low electric permittivity value. It is consistent with the true scene, where oil is distributed all over the core. The referred saturation distributions of the 3 slides of water, oil, and gas are shown in Figure 20, which are consistent with the electrical parameter distributions shown in Figure 19.

Then, the following is the air flooding water process, where water is almost all over the core, and Figure 21 shows that the core is characterized by high electric permittivity and high conductivity values. The referred saturation distributions of the 3 slides of water, oil, and gas are shown in Figure 22, which are consistent with the electrical parameter distributions in Figure 21.

Finally, Figure 23 shows the final stage of the air flooding water process, where it is characterized by low conductivity and low electric permittivity. And the referred saturation distributions of the 3 slides of water, oil, and gas are shown in Figure 24, which are consistent with the electrical parameter distributions in Figure 23.

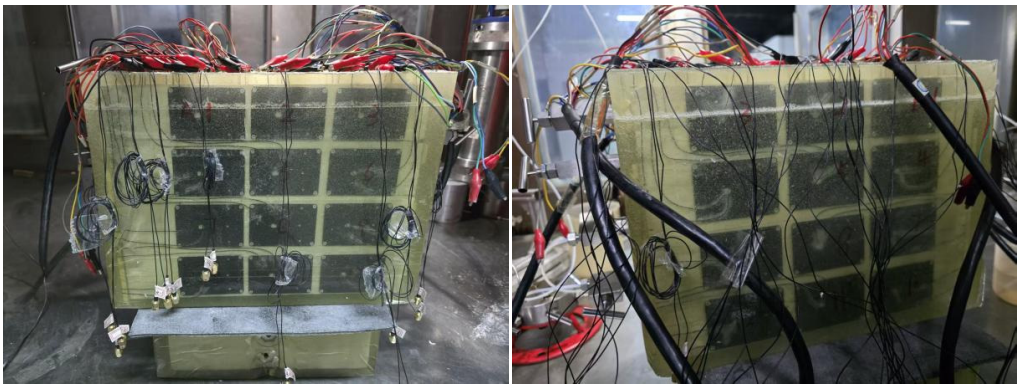

(**a**) (**b**)

Figure 18. The observation system of the physical core flooding experiment. (a) 16 transmitters distributed on one side of the core, (b) 16 receivers distributed in another side of the core.

 doi:10.20944/preprints202603.1920.v1

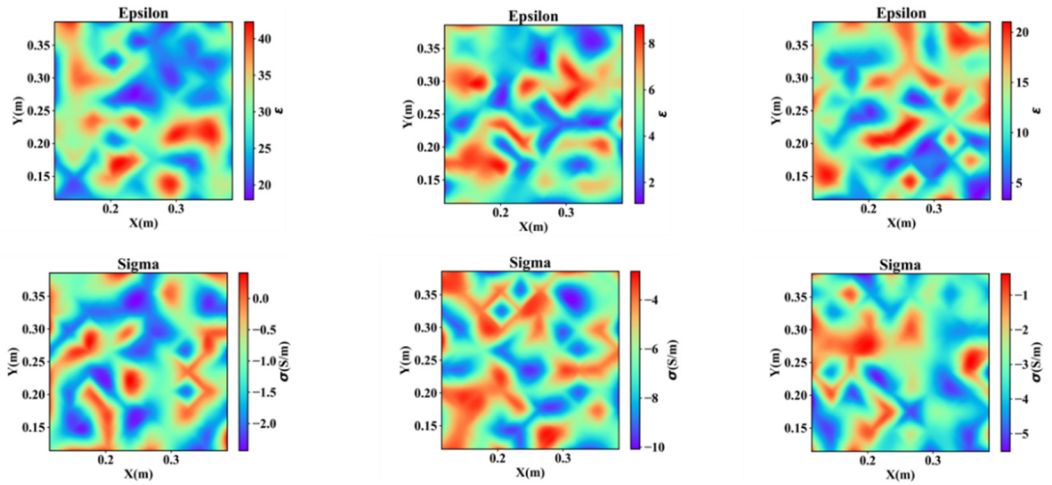

Figure 19. 2D inversion results in the starting stage of the water flooding oil experiment done in a laboratory rock core. The first row shows the variations of the electric permittivity distribution in different slices of the core, and the second row shows the variations of the conductivity distribution in different slices of the core.

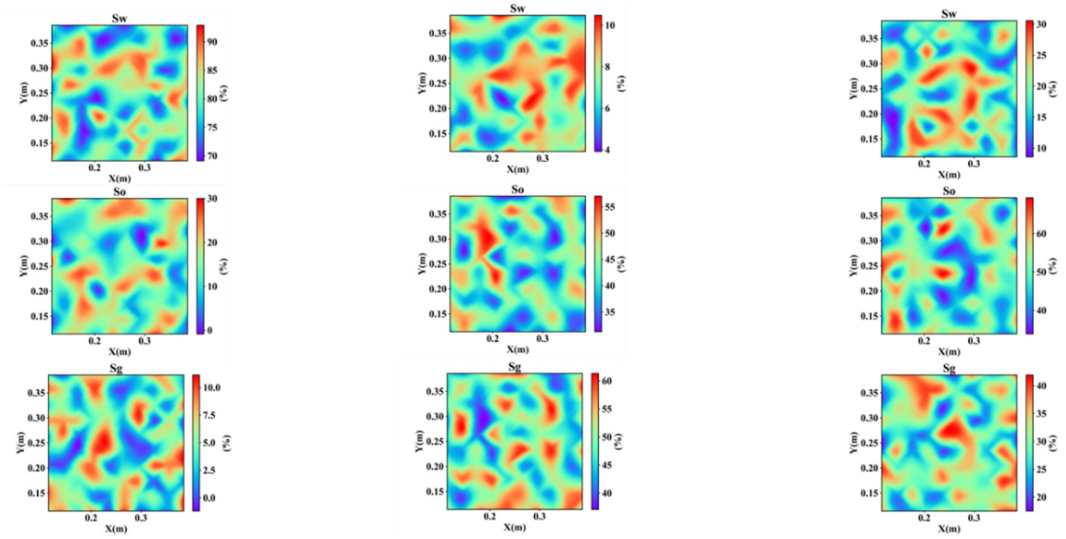

Figure 20. 2D saturation results in the starting stage of the water flooding oil experiment done in a laboratory rock core. The first row shows the water saturation distribution in different slices of the core, the second row shows the oil saturation distribution in different slices of the core, and the third row shows the gas saturation distribution in different slices of the core.

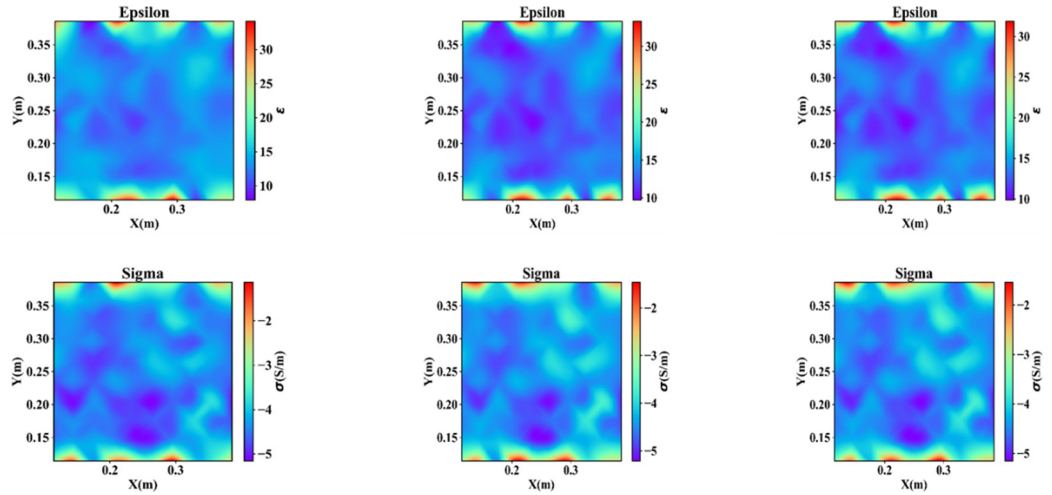

 doi:10.20944/preprints202603.1920.v1

Figure 21. 2D inversion results at the beginning of the air flooding water experiment done in a laboratory rock core. The first row shows the variations of the electric permittivity distribution in different slices of the core, and the second row shows the variations of the conductivity distribution in different slices of the core.

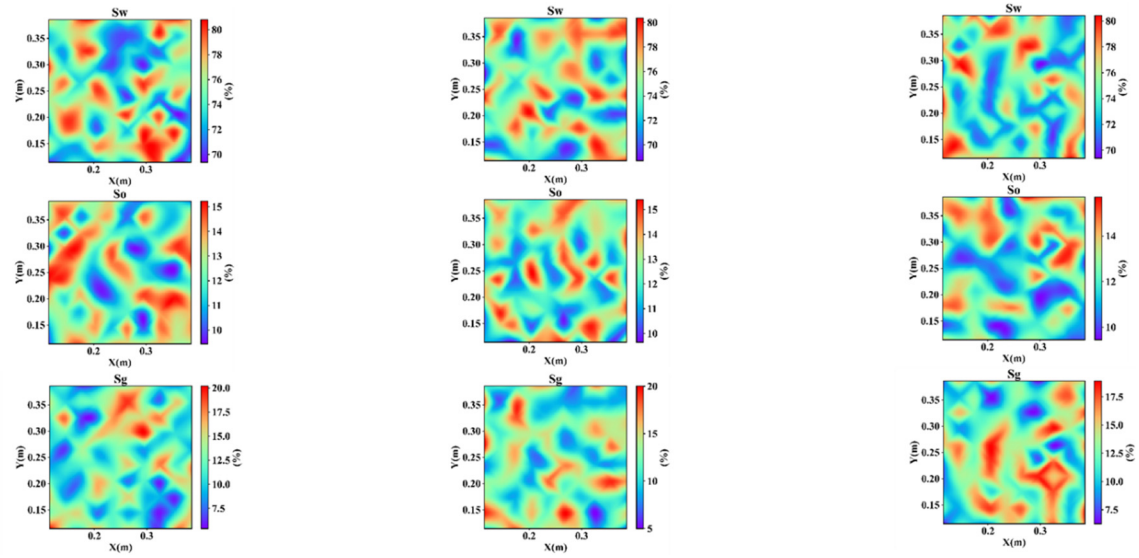

Figure 22. 2D saturation results in the starting stage of the air flooding water experiment done in a laboratory rock core. The first row shows the water saturation distribution in different slices of the core, the second row shows the oil saturation distribution in different slices of the core, and the third row shows the gas saturation distribution in different slices of the core.

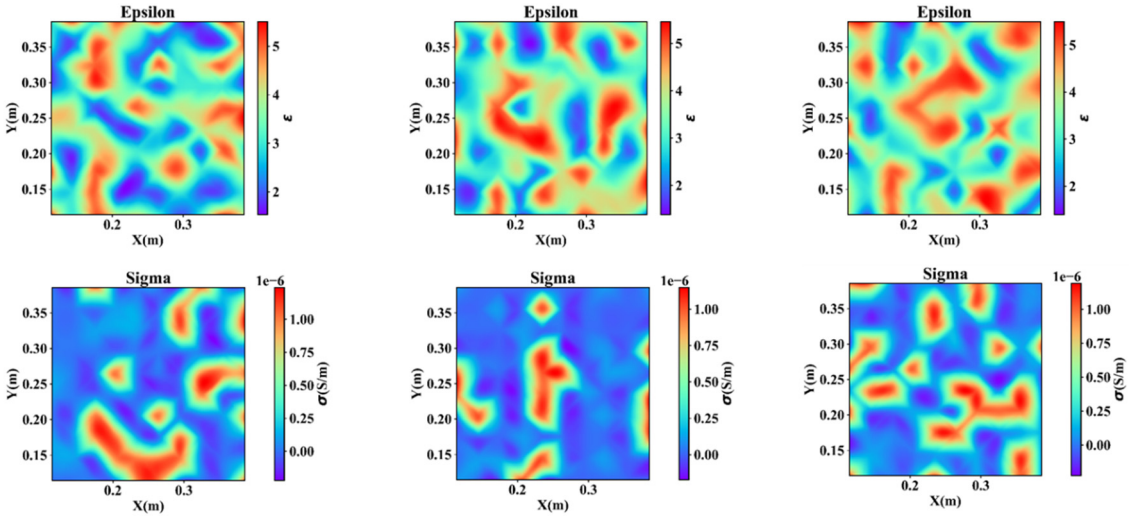

Figure 23. 2D inversion results at the end of the air flooding water experiment done in a laboratory rock core. The first row shows the variations of the electric permittivity distribution in different slices of the core, and the second row shows the variations of the conductivity distribution in different slices of the core.

 doi:10.20944/preprints202603.1920.v1

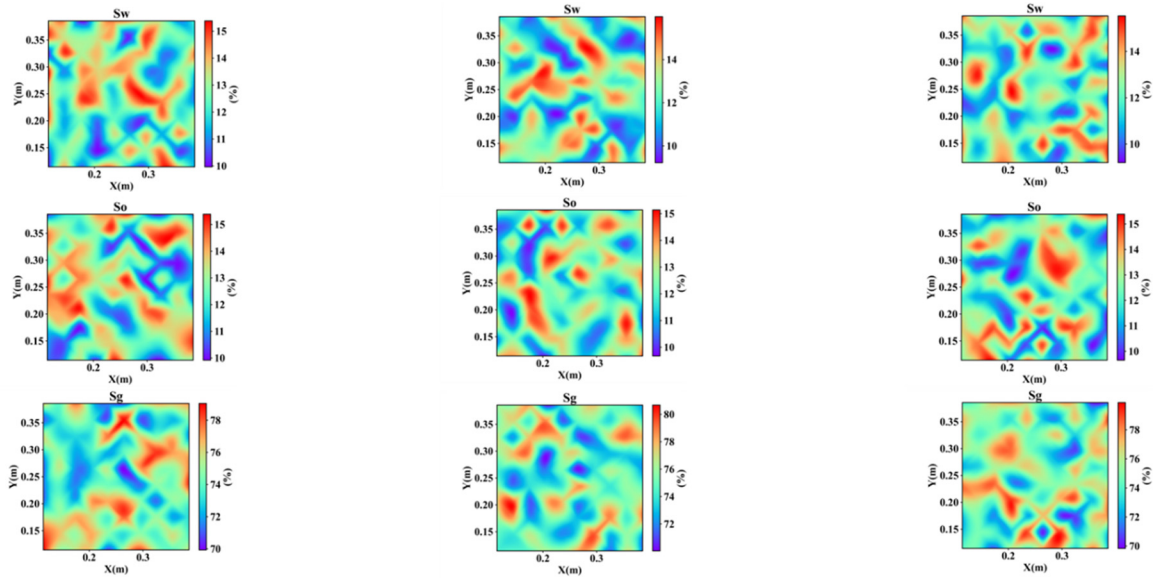

Figure 24. 2D saturation results in the end stage of the gas flooding water experiment done in a laboratory rock core. The first row shows the water saturation distribution in different slices of the core, the second row shows the oil saturation distribution in different slices of the core, and the third row shows the gas saturation distribution in different slices of the core.

5. Conclusions

The U-Net-based GPR inversion method provides an efficient and practical technical path for monitoring the reservoir flooding process. This study shows that the U-Net-based 2D GPR inversion method has stable and practical performances in numerical experiments. The network can clearly reconstruct the electrical parameter distributions of the oil, water, and gas in the sandstone. The inversion error for the dielectric constant is generally small, and the conductivity reconstruction also reaches engineering-acceptable precision in most areas. With an end-to-end learning framework, the inversion process is very fast (the inversion of 10,000 samples takes approximately 6 seconds), enabling real-time monitoring of the flooding process.

The performance of the proposed method was also tested by a physical core experiment, which implements the water flooding oil and gas flooding water process. The laboratory core experiment shows that the proposed method could successfully recover the variations of the electric permittivity and conductivities in the flooding processes.

The advantages of the method are as, (1) significantly improving the speed of data-to-model conversion, facilitating continuous observation and real-time imaging in high-frequency monitoring scenarios, (2) effectively capturing complex nonlinear coupling relationships through data-driven feature learning, (3) the model structure is easily extendable, and can be combined with multi-transmitter, multi-receiver, different polarization, or multi-frequency information, improving its adaptability in complex strata.

Author Contributions: The authors confirm contribution to the paper as follows: Conceptualization, Jie Zhang; methodology, Maolei Cui; validation, Rui Wang; formal analysis, Jie Zhang; investigation, Maolei Cui; resources, Rui Wang; data curation, Maolei Cui; writing—original draft preparation, Jie Zhang; writing—review and editing, Jie Zhang; visualization, Rui Wang; supervision, Jie Zhang; project administration, Jie Zhang. All authors reviewed the results and approved the final version of the manuscript.

Funding: This work is mainly supported by the National Science and Technology Major Project of China (Grant No. 2024ZD 1004302) and the Key Scientific and Technological Research project of SINOPEC (Grant No. P25186).

 doi:10.20944/preprints202603.1920.v1

Institutional Review Board Statement: (1) Whether or not the study included human or animal subjects. In all cases, the ethical approval status of the work should be stated in the ethical approval statement. (2) The committee which approved the study. (3) The compliance documents. What policies, declarations, acts, etc. (4) Persistent identifier: reference or approval number. Include the registration ID/reference number if applicable. (5) "Not applicable." for studies not involving humans or animals.

Data Availability Statement: (1) Data openly available in a public repository. (2) "The data that support the findings of this study are openly available." (3) Data available within the article or its Supplementary Materials. (4) "The authors confirm that the data supporting the findings of this study are available within the article [and/or] its Supplementary Materials." (5) Data available on request from the authors. (6) "The data that support the findings of this study are available from the Corresponding Author, [author initials], upon reasonable request." (7) Data not available due to [ethical/legal/commercial] restrictions. (8) "Due to the nature of this research, participants of this study did not agree for their data to be shared publicly, so supporting data is not available." (9) "Not applicable." (This article does not involve data availability, and this section is not applicable).

Acknowledgments: The authors would like to thank Dr. Pengfei Liang from Institute of Geology and Geophysics, Chinese Academy of Sciences to support this study.

Conflicts of Interest: The authors declare no conflicts of interest to report regarding the present study.

References

1. G. E. Archie, "The electrical resistivity log as an aid in determining some reservoir characteristics," Transactions of the American Institute of Mining, Metallurgical, and Petroleum Engineers, vol. 146, no. 1, pp. 54–62, 1942. https://doi.org/10.2118/942054-G.
2. J. H. Bradford, and W. Barrash, "Measuring water content heterogeneity using multifold GPR with reflection tomography," *Vadose Zone Journal*, vol. 7, no. 1, pp. 184–193, 2008. https://doi.org/10.2136/vzj2006.0160.
3. N. J. Cassidy, "Ground penetrating radar data processing, modelling and analysis," *In Elsevier Handbook of Geophysical Exploration,* Elsevier, 2009, pp. 141–176. https://doi.org/10.1016/B978-0-444-53348-7.00005-3 .
4. Y. Chen, F. Li, and S. Zhou, "New asphalt pavement dielectric constant inversion net based on improved gated attention for ground penetrating radar," *IEEE Transactions on Geoscience and Remote Sensing*, vol. 62, pp. 1–11. https://doi.org/10.1109/TGRS.2024.3496881.
5. C. Gao, J. Jia, W. Fan, S. Chen, T. Hu, X. Wang, et al, "Optimization of CO_2 flooding under dual goals of oil recovery and CO_2 storage: Numerical case studies of the first-ever CCUS pilot in Changqing Oilfield," *Geoenergy Science and Engineering*, vol. 240, no. 11, 2024. https://doi.org/10.1016/j.geoen.2024.213063.
6. D. P. Kingma, and J. Ba, "Adam: A method for stochastic optimization," *arXiv Preprint,* 2014. *https://doi.org/10.48550/arXiv.1412.6980*.
7. R. L. Kleinberg, "NMR measurement of petrophysical properties," *Concepts in Magnetic Resonance,* vol. 13, no. 6, pp. 404-406, 2001. https://doi.org/10.1002/cmr.1027.
8. W. Liu, X. Yang, H. Wang, L. Ding and W. Xu, "Forward simulation of GPR detection for irregular concealed distresses of road pavement based on the FDTD method," *Journal of Transportation Engineering, Part B: Pavements*, vol. 151, no. 2, 2025. https://doi.org/10.1061/JPEODX.PVENG-1671.
9. Q. Meng, L. Guo, S. Zhang, H. Lou and R. Li, "Deep learning in gravity research: A review," *Journal of Earth Science*, vol. 36, no. 4, pp. 1808–1819, 2025. https://doi.org/10.1007/s12583-023-1926-x.
10. A. Paszke, S. Gross, F. Massa, A. Lerer, J. Bradbury, G. Chanan, et al, "PyTorch: An imperative style, high-performance deep learning library," *Advances in Neural Information Processing Systems*, vol. 32, pp. 8024–8035, 2019. https://doi.org/10.48550/arXiv.1912.01703.
11. C. Warren, A. Giannopoulos, and I. Giannakis, "gprMax: Open source software to simulate electromagnetic wave propagation for ground penetrating radar," *Computer Physics Communications*, vol. 209, pp. 163–170, 2016. https://doi.org/10.1016/j.cpc.2016.08.020.
12. D. Wildenschild, and A. P. Sheppard, "X-ray imaging and analysis techniques for quantifying pore-scale structure and processes in subsurface porous medium systems," *Advances in Water Resources*, vol. 51, pp. 217–246, 2013. https://doi.org/10.1016/j.advwatres.2012.07.018 .

 doi:10.20944/preprints202603.1920.v1

13. Q. Zhen, Q. Di, P. Liang, et al, "An open-source code of the full-waveform inversion method verified by the synthetic GPR data to monitor the CO_2 flooding," *Journal of Geophysics and Engineering*, vol. 22, no. 6, pp. 1754–1767, 2025. https://doi.org/10.1093/jge/gxaf106.
14. T. Song, W. Zhu, Q. Chen, and M. Yue. "Uncertainty Quantification of CO_2 Flooding in Low-Permeability Oil Reservoirs Based on Interpretable Machine Learning." *Petroleum Science and Technology*, June, 1–25, 2025. https://doi.org/10.1080/10916466.2025.2522742.
15. S. Zhang and N. Zhou, "Extraction of Multiple Electrical Parameters From IP-Affected Transient Electromagnetic Data Based on LSTM-ResNet," in *IEEE Transactions on Geoscience and Remote Sensing*, vol. 61, pp. 1-14, 2023, Art no. 4501614, https://doi.org/10.1109/TGRS.2023.3266258.